Integrated Shape and Trajectory Optimisation of Hypersonic Waveriders

Agante de Carvalho, J.R.; Mooij, E.

DOI
10.2514/6.2024-0156

Publication date
2024

Document Version
Final published version

Published in
Proceedings of the AIAA SCITECH 2024 Forum

10.2514/6.2024-0156

Integrated Shape and Trajectory Optimisation of Hypersonic Waveriders

José Carvalho* and Erwin Mooij†
Delft University of Technology, Faculty of Aerospace Engineering, Delft, The Netherlands

This research performs a surrogate-assisted shape optimisation of hypersonic waveriders, where the trajectories of each shape are optimised with a multi-objective evolutionary algorithm for heat-load and cross-range. A study on the best evolutionary algorithm, node control strategy for angle of attack and bank angle profiles, and population size to use in the trajectory optimisation phase, are identified. The aerodynamics of the waveriders is computed with a new local surface inclination method blending the modified Newtonian and tangent wedge solutions, while the convective heat flux is computed for the leading edges using the Newton-Kays engineering model. Shape variability is introduced according to the layout of central composite designs, and analysis of variance is applied to identify the shape features driving the two objectives. Shock angle, leading edge radius and overall vehicle dimensions are the strongest drivers, while details on the planform shape are less relevant and should be left for posterior studies. The surrogates are a good approximation of the true fitness functions, so they were optimised in a single-objective framework, producing two optimal waverider designs.

Nomenclature

α	=	Angle of attack (rad)
β	=	Shock angle (rad)
C_{bf}	=	Body flap chord length (m)
C_e	=	Elevon chord length (m)
C_D	=	Drag force coefficient (-)
C_L	=	Lift force coefficient (-)
C_m	=	Pitch moment coefficient (-)
C_p	=	Pressure coefficient (-)
δ	=	Latitude (rad)
e_1, e_2, ω	=	Rational Bézier curve weights (-)
f, $\boldsymbol{f}$	=	Generic functions (-)
g	=	Gravitational acceleration (= 9.80665 m/s^2)
γ	=	Specific heat ratio (= 1.4), flight path angle (rad)
h	=	Altitude (m)
L	=	Waverider length (m)
m	=	Mass (kg)
M_∞	=	Free-stream Mach number (-)
$(M_\infty)_d$	=	Design Mach number (-)
μ_e	=	Earth's gravitational parameter (= $3.98600441 \times 10^{14}$ m^3/s^2)
$\dot{q}$	=	Convective heat flux (W/m^2)
Q	=	Heat load (J)
r	=	Leading edge radius (m)
r_e	=	Earth's equatorial radius (= 6378000 m)
S_{ref}	=	Aerodynamic reference area (m^2)
σ	=	Bank angle (rad)
θ	=	Wedge angle (rad), Inclination angle (rad)
τ	=	Longitude (rad)

*MSc Student, Astrodynamics and Space Missions; currently: GNC Engineer, GMV, Portugal, jose.carvalho@gmv.com.
†Associate Professor, Astrodynamics and Space Missions, e.mooij@tudelft.nl, AIAA Associate Fellow.

V_E = Entry velocity (m/s)
w_1 = Fuselage half width (m)
w_2 = Wing semi-span (m)
χ_E = Entry heading angle (rad)

I. Introduction and Motivation

Large satellite constellations are becoming a reality, and the growing number of spacecraft to be launched to orbits with different inclinations and altitudes raises the need for a highly flexible and frequently requested satellite launch service. It is in such conditions that a reusable concept becomes economically advantageous with respect to expendable systems, as noted in [1]. Despite their complexity and absence from the current launch vehicle market, reusable space-plane concepts are more flexible than their rocket counterparts. The superior control over the aerodynamic forces allows mission recall in case a payload problem is detected during ascent, and a larger number of landing sites becomes accessible when re-entering from a successful launch, reducing the turnaround time and costs.

Landing flexibility is strongly driven by the lift-to-drag ratio at hypersonic speeds. Waveriders are a sub-class of lifting-bodies with lift-to-drag ratios that are superior to conventional hypersonic configurations, so they have the potential to become a competitive operational launch vehicle. Such idea was already pursued in the 1980s with the National Aero-Space Plane and its technology demonstrator project, the Rockwell X-30.

However, pure waverider shapes are not realistic entry vehicles for a myriad of reasons. First, they rely on sharp leading edges, which have to be rounded off so that they can withstand the aerodynamic heat flux, an operation that inevitably degrades the aerodynamic performance at hypersonic speeds. A second issue is that waveriders are designed for specific flight conditions, while in a re-entry scenario they are constantly flying at off-design conditions. Without intelligent vehicle design, this can result in the degradation of the flight performance and bring complications to the thermal protection system design. Another concern is the lack of aerodynamic surfaces to trim and control the vehicle.

These concerns motivate the development of a modified waverider shape and of a framework to understand how its design should be modified and optimised, considering the trade-off between heat load and flight range that is commonly made for re-entry missions. Shape variability leads to variability in the achievable and optimal re-entry flight profiles. To respect such coupling, a joint shape and trajectory optimisation approach will be adopted.

This approach will not be applied to an operational vehicle, but rather to a down-sized technology demonstrator, which is likely needed to mitigate development risks and costs. The scope of the research will be limited to the hypersonic flight regime, as it is typically the most demanding segment of the entry [2].

II. Methodology

A. Vehicle Design

First, a baseline wedge-derived waverider will be established: a caret wing [3] split in half in the symmetry plane and then joined together by a wedge that acts as a fuselage, as shown in Fig. 1. Then, the upper surface will be displaced upwards to accommodate blunt leading edges, which corresponds to the "material addition method" described in [4]. The upper side of the lateral parts of the vehicles will be removed to facilitate the integration of elevons and promote vortex lift at lower speeds, generating wing-like features. A body flap will then be attached to the central portion of the trailing edge of the fuselage.

The waverider shape will be optimised using the Response Surface Methodology. For this, an array of shapes is generated according to the layout of central composite designs. Shape variability is obtained by varying the values of ten independent variables. An α of 2 was chosen and, following the recommendation of [5] for designs with more than five independent variables, axial points are repeated twice, amounting to 189 runs. This choice improves the prediction variance and it suited for this research since each vehicle will undergo a numerical trajectory optimisation process using genetic algorithms that have a probabilistic component.

The independent variables are the vehicle length, L, fuselage width, w_1, wing span, w_2, two weights controlling the planform shape, e_1 and e_2, leading edge radius, r, a weight controlling the leading edge cross-section, ω (as done in [6]), shock angle β, and the body flap and elevon chord lengths, C_b and C_e, respectively. The domain for optimisation is a 10-D hypercube, where the physical limits for each variable are shown in Table 1.

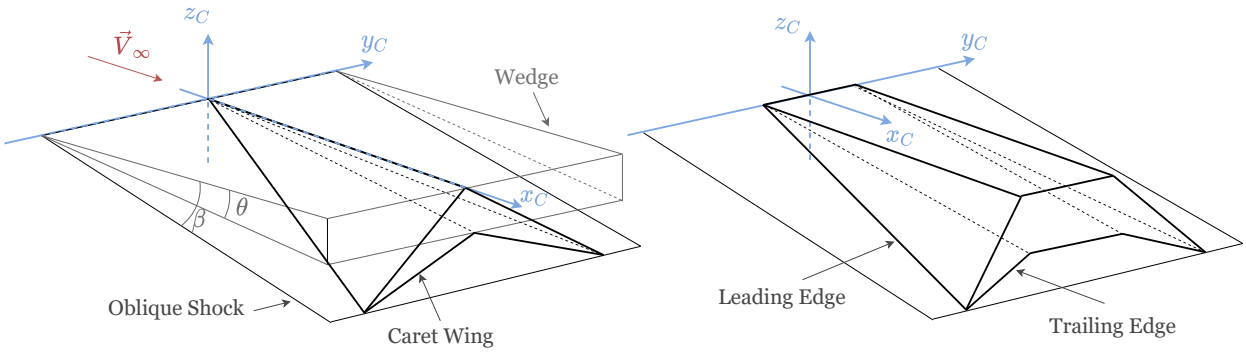

Fig. 1 Nonweiler's original (left) and modified (right) caret wing.

Table 1 Design variable ranges.

	L	w_1	w_2	e_1	e_2	r	ω	β	C_e	C_{bf}
Unit	[mm]	[mm]	[mm]	[-]	[-]	[mm]	[-]	[deg]	[mm]	[mm]
Min	2200	300	325	0.50	0.30	23	0.08	12.5	200	200
Max	4000	600	600	1.2	0.76	38	0.13	20.0	450	450

The planform of the vehicles is controlled by a rational Bézier curve of the form

$$\boldsymbol{B}(t) = \frac{\sum_{i=0}^{n} \omega_i B_{i,n}(t) \boldsymbol{P_i}}{\sum_{i=0}^{n} \omega_i B_{i,n}(t)} \tag{1}$$

where ω_i are the weights associated to each control point $\boldsymbol{P_i}$, and

$$B_{i,n} = \frac{n!}{i!(n-i)!} t^i (1-t)^i \tag{2}$$

are the Bernstein polynomials of degree n, with $t \in [0, 1]$. In the present case, a curve of degree $n = 3$ is used, and the weights and coordinates of the points in the $X_C Y_C$ plane (see Fig. 1) are given by:

$$\mathbf{P}_0 = (0, w_1) \qquad \omega_0 = 1, \tag{3}$$

$$\mathbf{P}_1 = (0, w_1 + w_2) \qquad \omega_1 = e_1, \tag{4}$$

$$\mathbf{P}_2 = \left(\frac{4L}{5\cos\beta}, w_1 + e_2 w_2 \right) \qquad \omega_2 = 1, \tag{5}$$

$$\mathbf{P}_3 = \left(\frac{L}{\cos\beta}, w_1 + w_2 \right) \qquad \omega_3 = 1 \tag{6}$$

but $\mathbf{P}_2$ and $\mathbf{P}_3$ are rotated about the Y_C axis by the shock angle β, so that the leading edge rests on the oblique shock. Figure 2 shows the shape variability that e_1 and e_2 create for the axial and factorial portions of the design, using the ranges of Table 1. A larger e_1 adds more material to the front of the vehicle, while a decreasing e_2 will gradually change the planform from a gothic shape (shown in light and dark blue on the bottom image of Fig. 2) towards a combined gothic-delta shape (shown in gray and red).

The leading edge cross section is also described by a rational Bézier curve, but this time with $n = 2$. The control

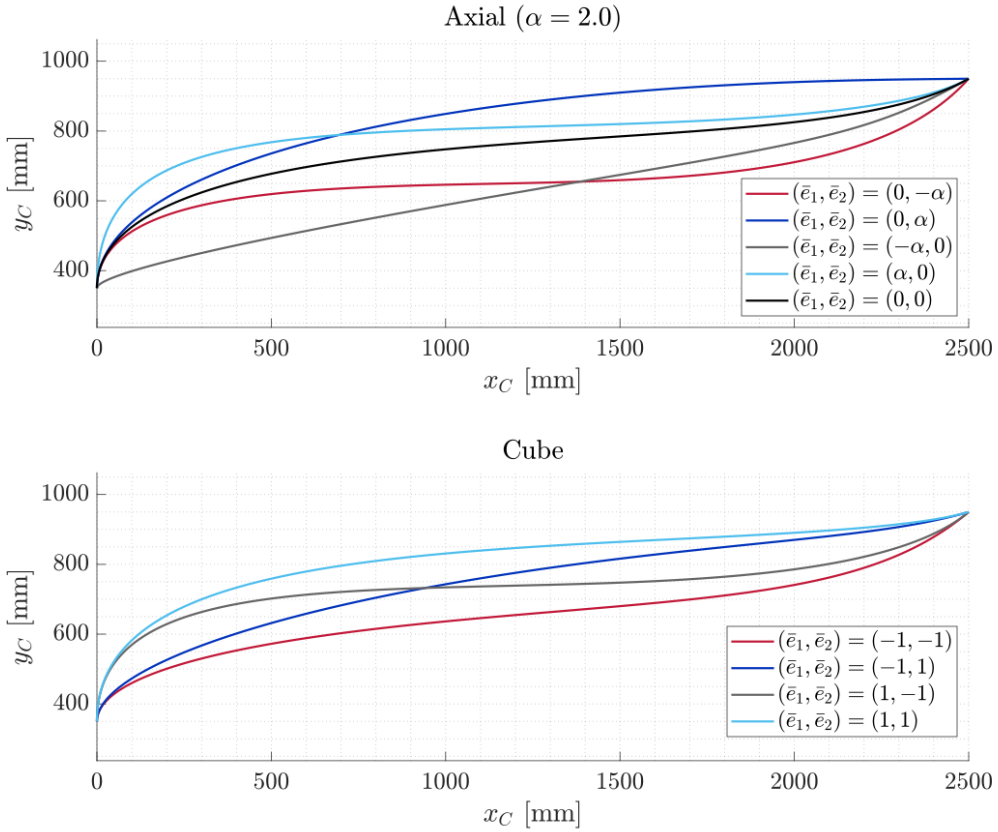

Fig. 2 Planform shape variability.

points are placed in the symmetry plane of the vehicle $X_C Z_C$, and their coordinates and weights are:

$$\mathbf{P}_0 = (0, 0) \qquad \omega_0 = 1, \tag{7}$$

$$\mathbf{P}_1 = \left(-\frac{2r}{\tan\theta}, 2r \right) \qquad \omega_1 = \omega, \tag{8}$$

$$\mathbf{P}_2 = (0, 2r) \qquad \omega_2 = 1, \tag{9}$$

where $\tan\theta$ is computed using,

$$\tan\theta = 2\cot\beta \frac{(M_\infty)_d^2 \sin^2\beta - 1}{(M_\infty)_d^2[\gamma + \cos(2\beta)] + 2} \tag{10}$$

a known relation from oblique shock-wave theory, where $(M_\infty)_d$ is the design Mach number. The physical limits for β shown in Table 1 were defined first, replicating the range of [7]. The range for ω was tweaked in a second step, and in a way that the optimal shapes found in [6] in the trade-off between drag coefficient and convective heat flux could be covered. Cross-section variability is shown in Fig. 3. Once defined, the cross-section is swept along the leading edge, from the symmetry plane at the nose towards the base plane of the waveriders.

The design Mach number will be set to a constant and large value for three reasons. First, it becomes easier to handle shape constraints, namely in the trailing edge of the wing-like features, where a linearisation is required to accommodate the hinges of the elevons. This issue is illustrated in Fig. 4, where the low $(M_\infty)_d$ design shows an intersection of the linearised bottom surface trailing edge with the upper surface trailing edge, making the design unfeasible. Secondly, as deduced from [8], it is a desirable feature to maintain good performance for a wide range of speeds. Finally, this design choice is expected to prevent the inwards motion of the shock attachment line, which could cause local hot spots that the thermal protection system is not capable to handle.

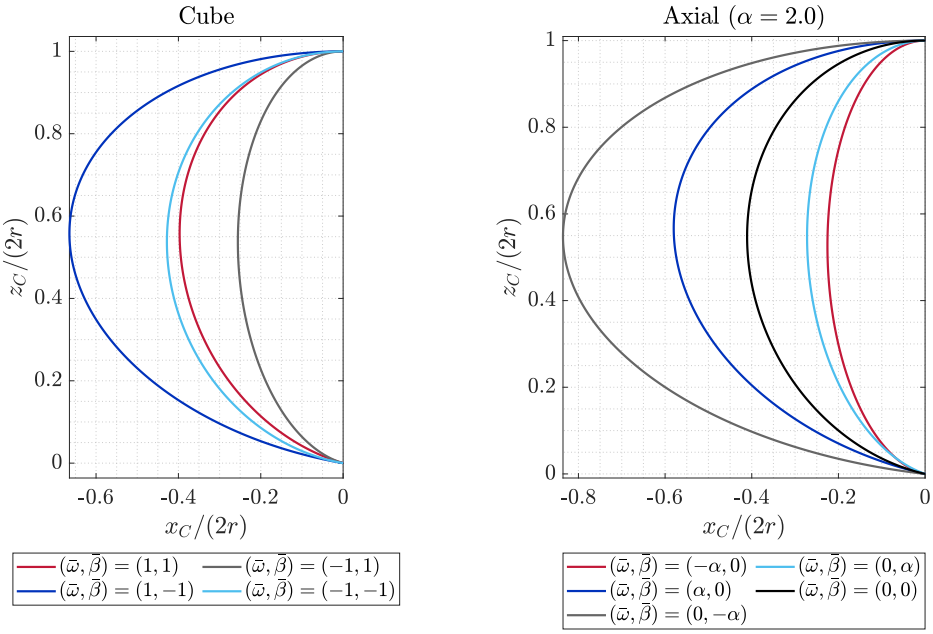

Fig. 3 Leading edge cross-sections

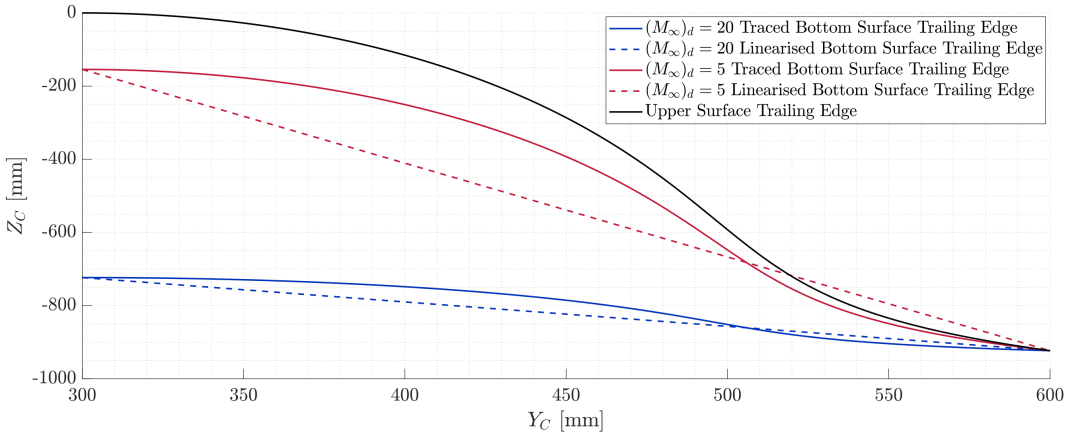

Fig. 4 Base plane view illustrating the effect of the design Mach number on the shape of the trailing edge.

The adopted mass model is based on the mass breakdown of Hyperion-II [9]. Although not a waverider, Hyperion-II was designed with similar dimensions, thermo-mechanical constraints, thermal protection system and recovery strategy, so it is a reasonable reference.

The model adopted here assumes that all waveriders have a fixed baseline mass, $m_0 = 80$ kg, that accounts for flight instrumentation, avionics and power units. The masses of an insulation blanket, m_b, and of the mechanical structure, m_s, scale with the surface area. They are respectively computed with

$$m_b = \sigma_b S_1 \tag{11}$$

$$m_s = t\left[S_2 \rho_{PM-2000} + (S_1 - S_2)\rho_{Ti}\right] \tag{12}$$

where $\sigma_b = 2$ kg/m^2 is the blanket's density, which is spread over the entire vehicle surface (of area S_1), S_2 is the surface area excluding the base plane, $t = 10^{-3}$ m is the thickness assumed for the structure, and $\rho_{PM-2000} = 7180$ kg/m^3, $\rho_{Ti} = 4430$ kg/m^3 are the densities of the PM-2000 alloy and Titanium, respectively.

The mass of the actuators, m_c, scales with the size of the control surfaces:

$$m_c = 2\sigma_c \left[C_{bf} w_1 + 0.9 C_e w_2 \right] \tag{13}$$

where $\sigma_c = 22$ kg/m^2 is a derived area density for the control surfaces.

Letting $m_{bp} = m_0 + m_s + m_b + m_c$, the mass of the parachute is estimated with

$$m_p = 3.1 \left(\frac{m_{bp}}{100} \right) + 1.2 \left(\frac{m_{bp}}{100} \right)^{1.5} + 1.5 \tag{14}$$

where the first term and second terms are respectively used to scale the masses of the canopies and parachute lines with the mass of the vehicle, and the last term represents the masses of deployment mortars and other non-scalable components. The total mass of a vehicle is then $m = m_p + m_{bp}$.

While the mass of the sub-components is estimated individually, their placement on the vehicle is not defined and is beyond the scope of this research. Therefore, a uniform vehicle density is assumed when computing the original coordinates for the centre of mass.

B. Aerothermodynamics

Databases for the lift, drag and pitch moment coefficients are computed for all vehicles using a new local surface inclination method that blends the popular Modified Newtonian[10] and Tangent-Wedge[11] methods for windward panels. The same blending philosophy was adopted by [12] and [13] to describe the pressure distribution over blunted-edged wedges and blunted-edged waveriders, respectively. When compared with standard Modified Newtonian, this new strategy (here baptised as Modified Hankey) allows more accurate pressure coefficient estimates on regions with small inclinations, which comprise the majority of the windward side of waveriders at small α, but approximates the Modified Newtonian solution in blunted regions such as the leading edges or the waverider under-surfaces at large α. The proposed expression for the pressure coefficient is:

$$C_p = C_p^N (\sin\theta)^{1/2} + C_p^W (1 - \sin\theta)^2 \tag{15}$$

where C_p^N is the modified Newtonian solution,

$$C_p^N = \frac{2}{\gamma M_\infty^2} \left[\left(\frac{(\gamma+1)^2 M_\infty^2}{4\gamma M_\infty^2 - 2(\gamma-1)} \right)^{\frac{\gamma}{\gamma-1}} \left(\frac{1 - \gamma + 2\gamma M_\infty^2}{\gamma + 1} \right) - 1 \right] \sin^2\theta \tag{16}$$

as found in [10], and C_p^W is the pressure coefficient obtained with the tangent wedge solution taken from [11]:

$$C_p^W = \theta^2 \left[\frac{\gamma+1}{2} + \sqrt{\left(\frac{\gamma+1}{2} \right)^2 + \frac{4}{(M_\infty \theta)^2}} \right] \tag{17}$$

Figure 5 shows the pressure coefficient as a function of the inclination angle obtained with Eq. (15) (in grey) for three Mach numbers, and the same curves obtained with Eq. (16) (red), Eq. (17) (dark blue), and the empirical fit from [12] (light blue).

Pressure on leeward panels is computed with the ACM empirical model [14], but with the base pressure, C_{p_b}, replaced by Gabeaud's model [15]:

$$C_p = \max \left(\frac{\theta}{16 M_\infty^2}, C_{p_b} \right) \tag{18}$$

$$C_{p_b} = \frac{2}{\gamma M_\infty^2} \left[\left(\frac{2}{\gamma+1} \right)^{1.4} M_\infty^{-2.8} \left(\frac{2\gamma M_\infty^2 + 1 - \gamma}{\gamma + 1} \right) - 1 \right] \tag{19}$$

where θ is negative and given in degrees.

Convective heat-flux databases for the un-swept leading edge region of the vehicles (where the heat flux is expected to be the highest) are generated using the Newton-Kays model presented in [16] and adopted in [17] for a rapid shape optimisation study.

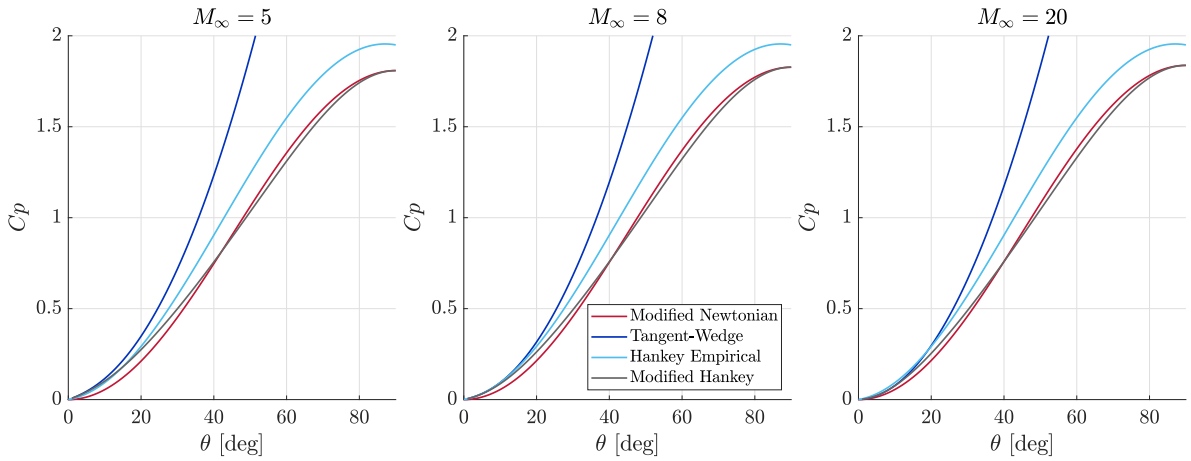

Fig. 5 Pressure coefficient as function of inclination

The leading edge cross-sections are discretised and the normal vectors are computed at each point. Then, the modified Newtonian model is used to compute the pressure coefficient at each node. The point of maximum pressure coefficient is taken as stagnation point. Once the pressure is known, the normal shock and isentropic flow relations are used to compute the temperature, velocity, density and viscosity at the edge of the boundary layer. Then, the reference temperature

$$T_r = T_e\left[1 + 0.032M_e^2 + 0.58\left(\frac{T_w}{T_e} - 1\right)\right] \tag{20}$$

as given in [10], is used to compute the reference dynamic viscosity and density. Viscosity is obtained from Sutherland's law, while the density is computed with the ideal gas law, under the assumption that $\mathrm{d}p/\mathrm{d}y \approx 0$ within the boundary layer.

The laminar heat flux is then computed using

$$\dot{q}(x) = C_1\left[\frac{(\rho_r V_e)^{C_2}\mu_r}{\int_0^x (\rho_r V_e)^{C_2} dx}\right]^{1/2} c_p(T_{aw} - T_w) \tag{21}$$

with $C_1 = 0.418$ and $C_2 = 1.87$ for $Pr = 0.7$, and where

$$T_{aw} = T_\infty\left(1 + \sqrt{Pr}\frac{M_\infty^2(\gamma - 1)}{2}\right) \tag{22}$$

is the adiabatic wall temperature, and an isothermal wall with $T_w = 400$ K is assumed.

The x coordinate in the integral is the distance along the surface measured from the stagnation point (where $x = 0$). There is a singularity at the stagnation point, but its effects on the heat flux profile can be minimised simply by using a finer grid, as shown in Fig. 6.

The heat flux profile is integrated along the surface of the unswept portion of the leading edge using

$$\dot{Q} = \int\int_S \dot{q}(x)dS = 2w_1\int_{x^-}^{x^+} \dot{q}(x)dx \tag{23}$$

where x^- and x^+ are the running lengths from the stagnation point to the two end points of the Bézier curve. The one-dimensional integral is evaluated numerically with the rectangle rule for an array of flight conditions, which allows $\dot{Q}$ to be linearly interpolated along the flight. This also allows the time integral of Eq. (23), that is, the heat load, to be computed from:

$$Q = \int_0^{t_F} \dot{Q}(t)dt \approx \Delta t \sum_{i=0}^{t_F/\Delta t} \dot{Q}(t_i) \tag{24}$$

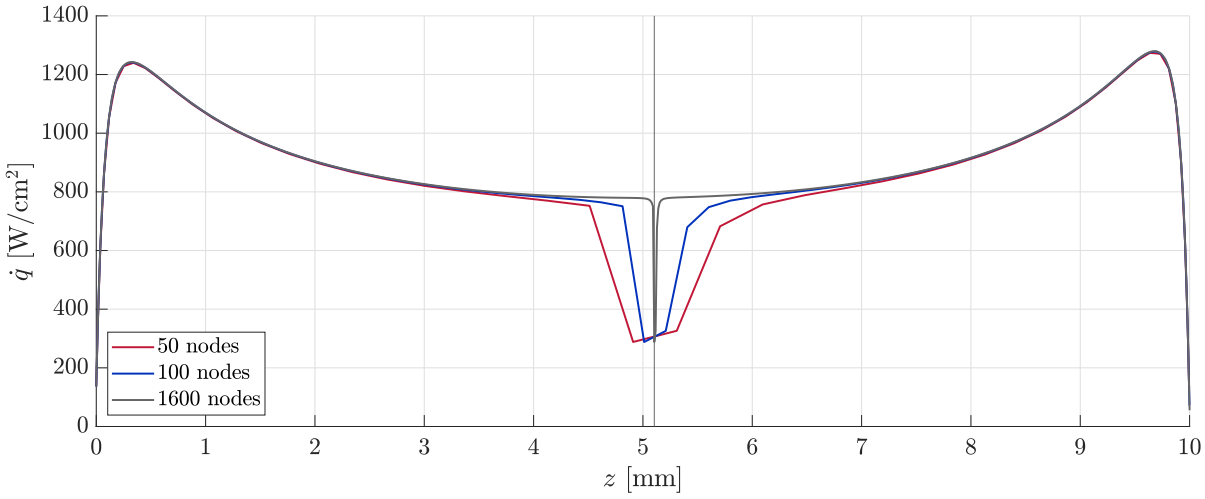

Fig. 6 Narrowing of the heat flux dip near the stagnation point (vertical line) with increasing node density.

C. Trajectory Optimisation

The re-entry trajectories of each vehicle start along the equator and will be numerically propagated and optimised for cross-range and heat load using MOEA/D with Tchebycheff decomposition [18]. The objective function is

$$\boldsymbol{f} = (-\delta_F, Q) \tag{25}$$

where Q is given in mega Joule and δ_F is the latitude (in radians) at the end of the propagation. Final latitude is used instead of the cross-range so that the first dimension of $\boldsymbol{f}$ has the same order of magnitude as the second (Q, which is expressed in mega Joule). If Q was given in Joule, the cross-range (in meters) should be used in the first dimension, as its order of magnitude would also be 10^6. Since MOEA/D works with norms in the objective space, having consistent orders of magnitude between the objectives is fundamental to avoid Pareto fronts skewed in favor of one of them (usually the one with the largest magnitude). This problem has already been recognised in [19].

The Cartesian position and velocity of the vehicles are propagated with a fixed-step Runge-Kutta integrator of fifth order, with $\Delta t = 1$s. A central body gravity field model perturbed by the J_2 term is used in combination with the US-76 atmosphere model. Earth is modeled as an oblate spheroid. The fixed entry conditions are:

$$h_E = 120 \text{ km}, \qquad V_E = 6500 \text{ m/s}$$
$$\chi_E = 90°, \qquad \tau_E = 0°, \qquad \delta_E = 0°$$

which corresponds to a sub-orbital entry along the equator. The entry flight path angle, $\gamma_E \in [-5°, -0.01°]$ is one of the independent variables to be optimised, but all vehicles start their flight with the same specific mechanical energy. The propagation stops when $M_\infty < 5 \vee h < 20$ km.

Bank angle and angle of attack profiles are generated using the node control strategy proposed in [20]. These angles are interpolated along the flight using cubic Hermite splines. The monotonically-decreasing independent variable used for interpolation is the specific energy

$$e = \frac{V^2}{2} - \frac{\mu_e}{R} + \frac{J_2 \mu_e r_e^2}{2R^3}(3\sin\delta - 1) \tag{26}$$

but normalised with e at entry conditions, so that it becomes bounded between 0 an 1. At the entry point, that is, $e/e_E = 1$, we fix $\alpha = 30°$ and $\sigma = 45°$, while at $e/e_E = 0$, $\alpha = \sigma = 0°$. During the flight, the sideslip angle is set to zero, $\alpha \in [0°, 40°]$, and $\sigma \in [0°, 90°]$.

The optimisation is split in two steps. In the first step, the independent variables are the coordinates of the interpolation nodes, the entry flight path angle, and the centre of mass location, while in the second step, all variables but the centre of mass are maintained. The region where the centre of mass is allowed to vary in the first step is a downscale of the triangular cross-section taken at the symmetry plane of the waverider. The centroid of the triangle coincides the original centre of mass, and the largest leg, parallel to X_C, has a length of $0.18L$.

The first optimisation step counts with a small number of iterations (50), as its purpose is to rapidly identify unfeasible configurations and iterate the physical (shape) design variable range. This process is repeated until the whole array of shapes is able to produce at least one feasible trajectory, and it culminated with the ranges shown in Table 1. In the second optimisation step, the centre of mass is removed from the optimisation variables to enhance convergence, and a higher number of iterations is used.

Pitch trim is enforced as constraint when the dynamic pressure is greater than 100 Pa, and the aerodynamic force contributions from the control surfaces are included in the dynamics. Further constraints include the maximum bank angle and angle of attack rates, respectively $|\dot{\sigma}| \leq 20°/s$, $|\dot{\alpha}| \leq 5°/s$, which are introduced since any real vehicle will take some time to respond to α and σ commands due to its inertia. The load factor, n, must satisfy

$$n = \frac{\sqrt{D^2 + L^2}}{mg} \leq 2.5 \tag{27}$$

and a maximum convective heat flux of 2 MW/m^2 is allowed. To avoid strong oscillations in thermo-mechanical loads, a maximum flight path angle of 0.15° is imposed.

To force the optimisation algorithms to find feasible domains within the design space, the following constraint handling strategy is applied. First, all individual constraint violations are mapped to a scalar. This scalar is computed similarly for all constraints except the trim, and intends to be a normalised value that is simultaneously proportional to the magnitude and duration of the constraint violation. For instance, the scalar associated with the g-load constraint is:

$$c_n = \frac{1}{2 t_F n_M} \int_0^{t_F} n(t) \left(1 + \frac{n(t) - n_M}{|n(t) - n_M|} \right) dt \tag{28}$$

where $n_M = 2.5$, and where the integral is evaluated with the rectangle rule and t_F is the time of flight. For the special case of the trim constraint, the scalar is given by

$$c_T = \frac{1}{t_F} \int_0^{t_F} \frac{C_m(t)}{|C_m(t)|} dt, \qquad \forall t : C_m(t) \neq 0 \tag{29}$$

so it is only proportional to the time during which the vehicle is not trimmable. All penalties are grouped together according to:

$$c_\epsilon = c_n + c_{\dot{q}} + c_\gamma + c_T + c_{\dot{\alpha}} + c_{\dot{\sigma}} \tag{30}$$

Whenever $c_\epsilon \neq 0$, a very large constant penalty term is added to c_ϵ, and the result is then added to each objective, Q and $-\delta_F$. This scheme is equivalent to the *feasible over unfeasible* method used in [2].

The results obtained with the selected optimisation algorithm were compared with two other options, NSGA-II [21] and MOEA/D with Boundary-Intersection decomposition. To characterise the performance of each algorithm, the trajectory of the nominal waverider (the shape at the centre of the design space) is optimised with 30 different seeds, and two quality indicators are computed for every run. The first, labelled here as I_1, is the overall Pareto spread indicator proposed in [22], while the second, I_2, is used to quantify the relative dominance between two Pareto sets, fitting into the family of hyper-area indicators that [23] classified as convergence indicators.

Given an n-dimensional Pareto-front approximation $\mathcal{A}$, the Pareto spread indicator is computed with:

$$I_1(\mathcal{A}) = \prod_{i=1}^{n} \frac{|F_i^I - F_i^N|}{R_i} \tag{31}$$

where

$$R_i = \max_{\boldsymbol{x} \in \mathcal{A}} f_i(\boldsymbol{x}) - \min_{\boldsymbol{x} \in \mathcal{A}} f_i(\boldsymbol{x}) \tag{32}$$

and where $\boldsymbol{F}^I$ and $\boldsymbol{F}^N$ are, respectively, the estimated ideal and nadir points, which are extracted from the minimum and maximum objective function values found among all non-dominated points created in the 90 runs of optimisation. Pareto sets that yield a higher I_1 are more spread out across the solution space, and are regarded superior in this sense. Here, both the value of I_1 averaged over the 30 seeds, and the thickness of its dispersion envelopes are considered. The latter provides additional information on convergence of the algorithms.

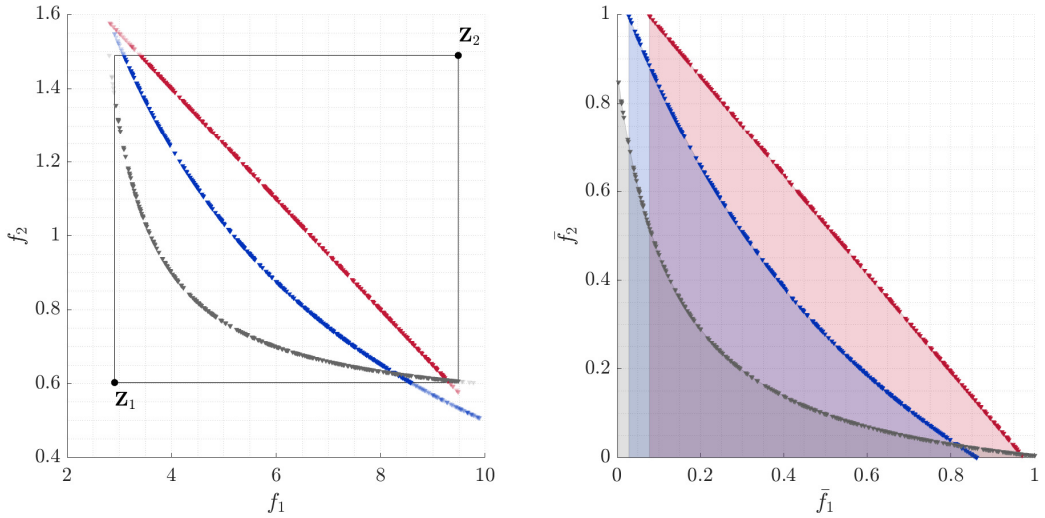

Fig. 7 Graphical representation of the steps required to compute I_2.

The second indicator focuses on the relative *depth* of Pareto-front approximations rather than the spread, so it works as a complement of I_1. To compute I_2, s Pareto-front approximations $\mathcal{A}_1, ..., \mathcal{A}_s$ are first merged together and used to compute two reference points $\mathbf{Z}_1$ and $\mathbf{Z}_2$. Formally, the coordinates of these points is given by:

$$Z_{1_i} = \max_{j=1,..,s} \left[\min_{\boldsymbol{x} \in \mathcal{A}_j} f_i(\boldsymbol{x}) \right] \tag{33}$$

$$Z_{2_i} = \min_{j=1,..,s} \left[\max_{\boldsymbol{x} \in \mathcal{A}_j} f_i(\boldsymbol{x}) \right] \tag{34}$$

In two-dimensions, $\mathbf{Z}_1$ and $\mathbf{Z}_2$ are in opposite ends of a rectangle in the objective space. All solutions outside this rectangle are removed from the respective sets, so that Pareto depth is only evaluated in a region that is common to all sets. In the second step, the objectives are normalised (individually for each dimension) using $\mathbf{Z}_1$ and $\mathbf{Z}_2$, so that they become bounded between 0 and 1. Finally, the area under each normalised Pareto-front is computed using the trapezoid rule. This three-step process is illustrated in Fig. 7. $I_2(\mathcal{A}_1) < I_2(\mathcal{A}_2)$, then solutions from set $\mathcal{A}_1$ will tend to be closer to the ideal point, hence they will dominate solutions from set $\mathcal{A}_2$.

Figure 8 shows the average of $I_1(g)$, as well as the dispersion envelopes of the 30 runs along the 500 generations. A population of 128 was used for all cases, and flight profiles were created with three freely moving interpolation nodes (plus the two fixed nodes at $e/e_E = 0$ and $e/e_E = 1$). MOEA/D with Tchebycheff decomposition is the option that better spreads the optimal solutions, but there are two signs of insufficient convergence: the first is that the I_1 average and its dispersion envelope have barely stabilised after 500 generations, and the second is that the envelope is still thick. MOEA/D with the Boundary Intersection approach is the worst performing option in what concerns the spreading of solutions, interrupting this process after about 200 generations, while NSGA-II, with a slightly better average spread after the 300th generation, produces the most inconsistent results, as deduced from the superior thickness of the dispersion envelope.

Figure 9 shows the evolution of the average value of I_2. It is clear that MOEA/D with Tchebycheff decomposition is again the best performing algorithm, while NSGA-II is the worst. The data shown in this figure correspond to single runs (seed 2), but similar results were obtained for the remaining 29 seeds. The three algorithms produce very similar Pareto-fronts in the short cross-range end, but the differences accentuate as the cross-range increases, both in terms of spread and depth. Under the light of such results, MOEA/D with Tchebycheff decomposition is the best option overall, so it is used for the coming discussions.

The best node control strategy was investigated next. Two node control strategies were compared, Non-Uniform Independent Node control (NUIN), where e/e_E can take any value within the range $[0.10, 0.99]$, and Uniform Independent Node Control (UIN), where the nodes are uniformly distributed in the e/e_E axis between 0 and 1. With NUIN, the optimisation algorithm is responsible for finding the optimal node locations. The higher flexibility of NUIN allows the

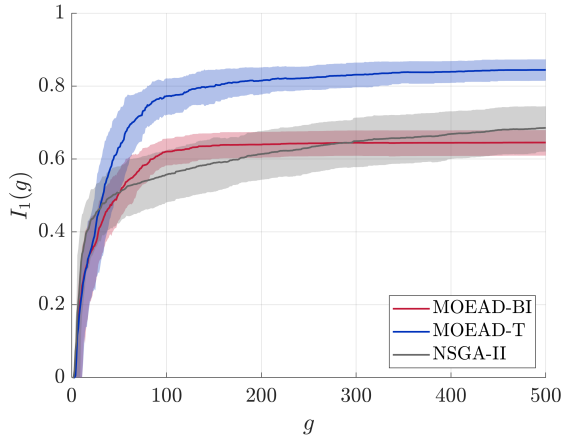

Fig. 8 I_1 indicator evolution for different optimisation algorithms.

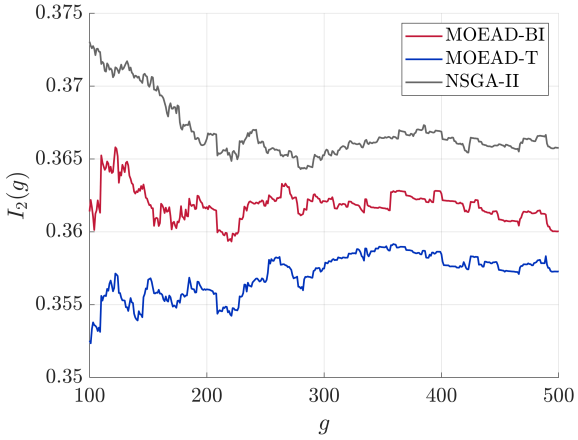

Fig. 9 I_2 indicator evolution for different optimisation algorithms.

optimiser to create more varied α and σ profiles, hence superior trajectories would be expected. On the other hand, the higher dimensionality of the optimisation problem may delay convergence. With fewer design variables, the advantage (disadvantage) pointed out for NUIN control - flexibility (convergence) - becomes a disadvantage (advantage) for UIN control.

The same procedure used in the algorithm trade-off was followed again, but this time each node control strategy was tested with three, four, and five interpolation nodes.

Figure 10 shows that the spread of the non-dominated front is superior for NUIN control with $N = 3$ and $N = 4$. The additional flexibility offered by NUIN seems to allow the optimiser to explore a broader range of solutions when N is small, but this effect fades away as the number of nodes increases. Increasing N leads to a decrease of the average I_1 for NUIN control, while the trend is inverted for UIN control. Cases with NUIN control have thicker $I_1(g)$ envelopes, indicating less consistent optimisation outputs, which signal convergence issues. Figure 10 also shows that convergence deteriorates with increasing N for both node control strategies, as the envelopes grow thicker.

The evolution of the average $I_2(g)$ shown in the left plot of Fig. 11 reveals that a higher N leads to higher quality Pareto-fronts in terms of depth, and that this trend is independent of the node control strategy. Furthermore, solutions generated with NUIN control tend to dominate the ones generated with UIN control. These relations are confirmed in the right plot of Fig. 11, where a close-up of the non-dominated fronts obtained with the six different optimiser configurations at $g = 500$ and for seed 2 is shown.

NUIN control with $N = 3$ and UIN control with $N = 4$ are two options that represent a trade-off between convergence and average I_1, the first option having better I_1 but thicker envelopes, and the latter having more favourable convergence, but lower average I_1. The UIN option with $N = 4$ is selected, as it will carry less noise to the response surface fitting stage.

In a final tuning step, the effect of the population size was analysed. Three options were tested: the original population of $P = 128$ individuals, $P = 64$, and $P = 256$. The optimisations were also extended to 2000 generations to assess if $g = 500$ was an appropriate stopping criterion.

Figure 12 shows that increasing the population size simultaneously improves the average value of the spread and the seed-consistency of the results for the same generation number g, but the improvements dissipate as g increases. In terms of Pareto depth, Fig. 13 reveals that no option is clearly superior to another. The option of $P = 256$ is thus selected. Figure 12 also shows there is little improvement in the thickness of the dispersion envelope for $P = 256$ after 700 generations, so this value would be an appropriate stopping criterion. However, the trajectory optimisation of a waverider shape different than the baseline used in this study may take more time to converge, so 1000 generations will be used.

D. Shape Optimisation

Once the second trajectory optimisation step is finished, each vehicle will be associated with a set of Pareto-optimal trajectories. For each Pareto set, the knee-point - that is, the solution closest to the ideal point in the objective space -

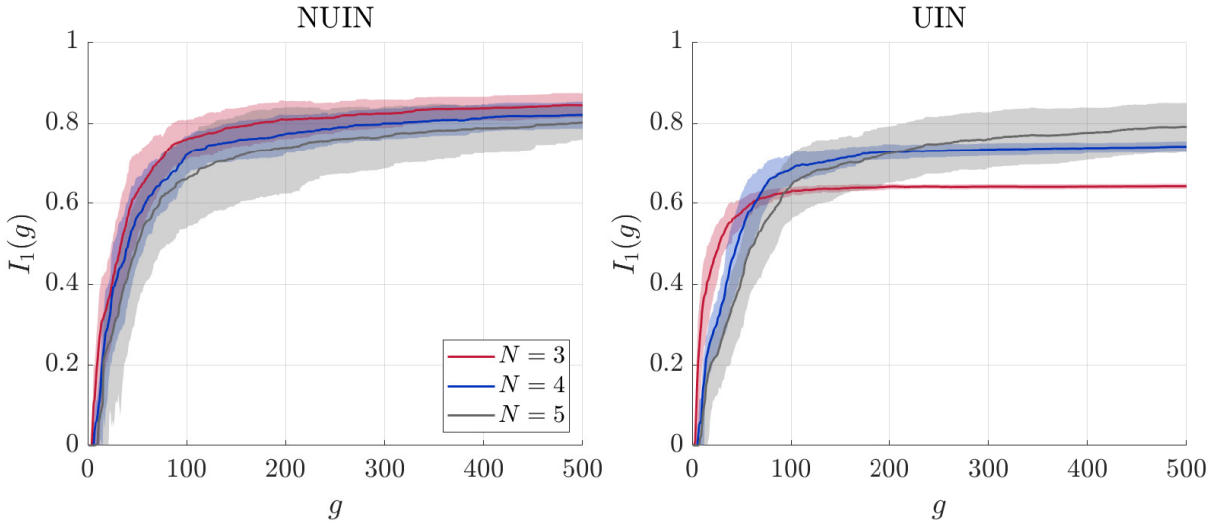

Fig. 10 $I_1(g)$ **evolution for NUIN and UIN control.**

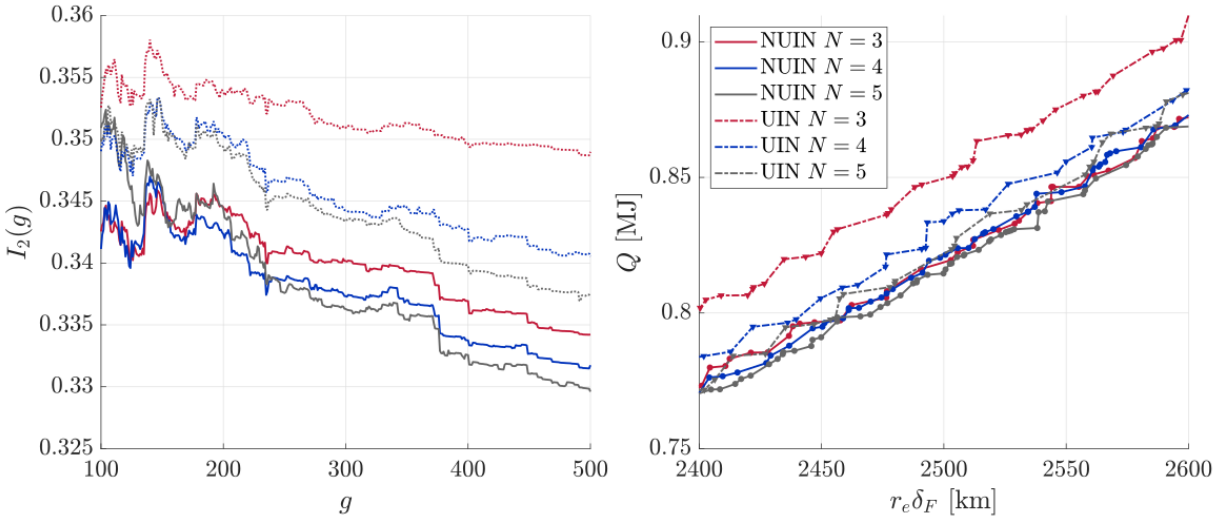

Fig. 11 $I_2(g)$ **evolution for NUIN and UIN control (left) and close-up on Pareto-fronts obtained for** $g = 500$ **and random seed 2 (right).**

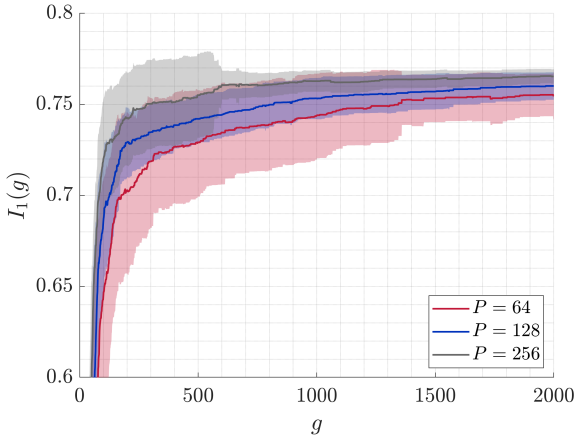

Fig. 12 $I_1(g)$ **evolution for different population sizes.**

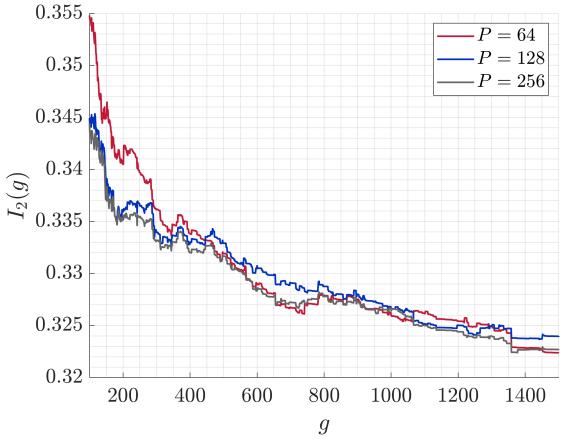

Fig. 13 $I_2(g)$ **evolution for different population sizes.**

will then be identified. The $(-r_e\delta_F, Q)$ coordinates of the knee points will be regarded as the observations for fitting the second order models relating the shape variables to the cross-range and heat load objectives. The fitted model for both objectives has the form:

$$\hat{y} = \hat{\beta}_0 + \sum_{i=1}^{k} \hat{\beta}_i \bar{x}_i + \sum_{i=1}^{k} \hat{\beta}_{ii} \bar{x}_i^2 + \sum_{i=1}^{k-1} \sum_{j=i+1}^{k} \hat{\beta}_{ij} \bar{x}_i \bar{x}_j \tag{35}$$

where $k = 10$, $\hat{\beta}_0$, $\hat{\beta}_i$ and $\hat{\beta}_{ij}$ are the coefficients to be estimated with ordinary least squares, and $\bar{x}_i$ are the normalised independent variables:

$$\bar{x}_i = \frac{2x_i - (x_{m_i} + x_{M_i})}{x_{M_i} - x_{m_i}}, \quad i = 1, ..., k \tag{36}$$

with $x_i \in [x_{m_i}, x_{M_i}]$, and where x_{m_i}, x_{M_i} take the values listed in Table 1. There are $p = 1 + 2k + k(k-1)/2 = 66$ coefficients to be estimated for each model.

When using ordinary least squares, the total sum of squares, S_T, which represents the sum of the squared deviations from the mean of the observations, that is,

$$S_T = \sum_{i=1}^{N_R} (y_i - \bar{y})^2 \tag{37}$$

with

$$\bar{y} = \frac{1}{N_R} \sum_{i=1}^{N_R} y_i \tag{38}$$

can be decomposed into an error sum of squares, S_E, and a regression sum of squares, S_R. Formally,

$$S_T = S_E + S_R = \sum_{i=1}^{N_R} (y_i - \hat{y}_i)^2 + \sum_{i=1}^{N_R} (\hat{y}_i - \bar{y})^2 \tag{39}$$

The factor sum of squares, S_f, with $f = 1, ..., p$, represents the reduction in S_E obtained by adding the term f to a predictive model that excludes it. Letting the latter be represented by $\hat{y}_f$, the factor sum of squares of factor f is formulated as:

$$S_f = \sum_{i=1}^{N_R} (y_i - (\hat{y}_f)_i)^2 - \sum_{i=1}^{N_R} (y_i - \hat{y}_i)^2 \tag{40}$$

where y_i represents an observation and $\hat{y}_i$ is prediction made with the complete model. The sensitivity of a response to a factor variation can be determined by computing the ratio between S_f and S_T,

$$P_f = S_f / S_T \times 100\% \tag{41}$$

similarly to what was done in [24].

Once they are available, the fitted models for $-r_e\delta_F$ and Q will be minimised independently using an interior point method, producing two optimal shapes. In a verification step, the predictions made for the objectives will be checked against their true values and if they fall within the 95% confidence intervals.

III. Validation Results

The computational fluid dynamics results from [25] are used to assess the accuracy of the panel method proposed in this study (Modified Hankey) when applied to caret waveriders with different degrees of leading edge bluntness (r/L ratios), and for an angle of attack ranging between zero and 15 degrees.

Results are shown in Fig. 14, side to side with the results obtained using the standard Modified Newtonian model. The accuracy of the force coefficients, C_D and C_L, is superior across the entire α range for all three vehicles when the Modified Hankey method is employed. Because the windward surfaces of the caret wings are dominated by panels with small inclinations, having just a slightly more accurate pressure model for such panels will translate into a substantially more accurate prediction of the force coefficients.

While both methods are able replicate the curve slopes for the pitching moment coefficient, C_m, the Modified Newtonian (Hankey) consistently under-predicts (over-predicts) the magnitude of this coefficient. Modified Hankey is, however, in slightly better agreement with the reference curve, which is particularly noticeable for $r/L = 0.008$. Under-predicting the magnitude of C_m when using a simplified inviscid aerodynamics model is not desirable, since real-gas effects are likely to render the estimated trim deflections too optimistic, as it was observed for the the Space Shuttle.

The implementation of the heat flux model was validated using the results from [26], where the peak convective heat

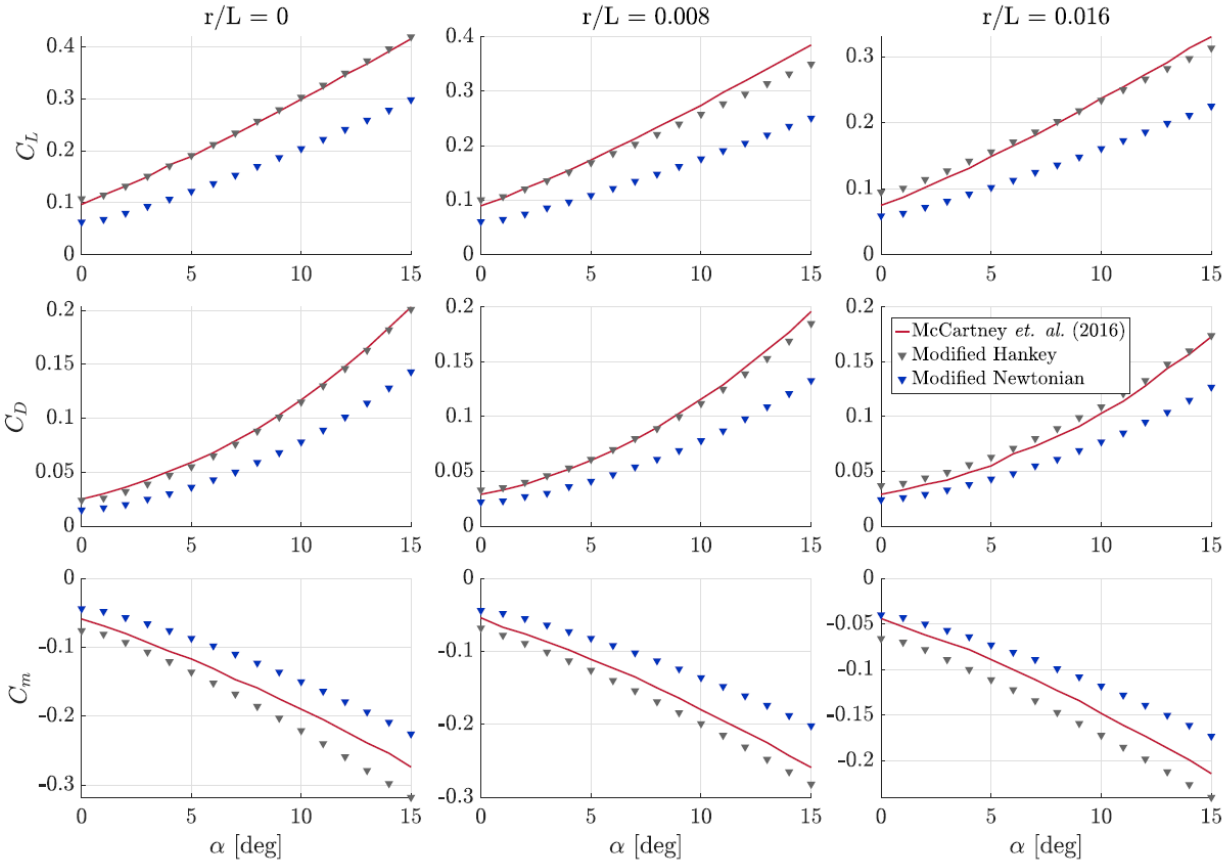

Fig. 14 Lift, drag and pitching moment coefficients as function of angle of attack for three caret waveriders.

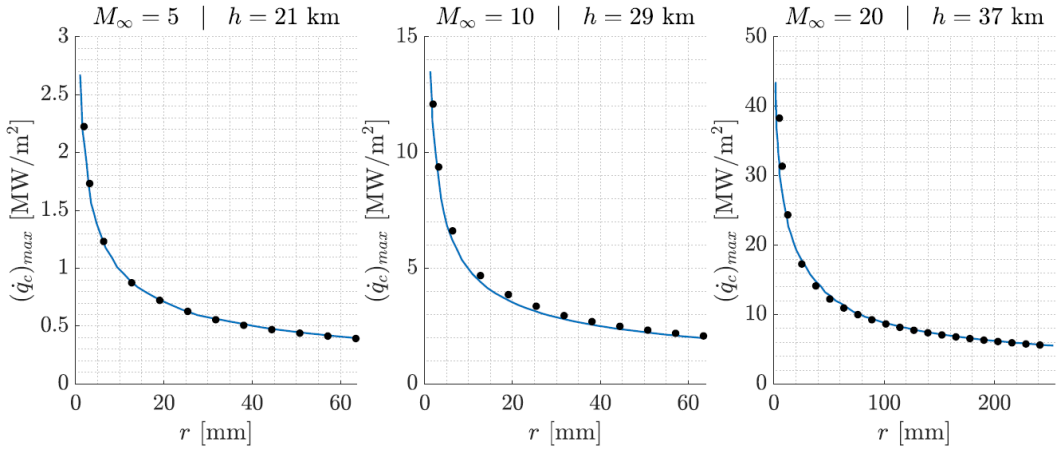

Fig. 15 Peak convective heat flux for cylinders with different radii at three flight conditions

flux was computed for several cylinders with distinct radii at three different flight conditions (the US-76 atmosphere model was used to translate h and M_∞ to the thermodynamic properties of the incoming flow). Figure 15 shows a very good agreement is obtained, with differences no larger than 6%.

In [27], a Navier-Stokes solver was used to characterise the heat flux profile on a cylinder with a radius of 2.5 mm immersed in $M_\infty = 6.5$ laminar flow, at an altitude of 25 km (free-stream properties again derived using the US-76 atmosphere model), and with a wall temperature of 300 K. The Newton-Kays model adopted here yields a peak heat flux of 3.675 MW/m^2, representing a relative difference of 2.7% with respect to the reference value of 3.579 MW/m^2.

IV. Optimisation Results

A closer look on the ensemble of Pareto fronts obtained in the trajectory optimisation sate reveals that vehicles with larger planform areas (large L, w_1 and w_2) tend to dominate vehicles with a smaller areas, and the relative cross-range improvement for the same heat load accentuates as cross-range increases. This trend can be visualised in Fig. 16, where the Pareto-fronts of the vehicles with minimum dimensions (red) are plotted against the Pareto-fronts of the vehicles with maximum dimensions (dark blue).

One of the possible reasons for this behaviour is that vehicles of maximum length have superior lift-to-drag ratios, as the L/D increases with decreasing r/L. A second explanation that does not invalidate the first one is the difference in the S_{ref}/m ratios found among the two groups. This ratio ranges between 0.0175 and 0.026 m$^2/kg$ for vehicles with maximum dimensions, while for the smallest vehicles it ranges between 0.0075 and 0.0145. The effect of the aerodynamic forces on the motion of the vehicle is proportional to S_{ref}/m. When more lift is available and its effectiveness in modifying the trajectory is higher, the optimiser is better equipped to modulate the force's vertical and horizontal components - which affect the time of flight and the change in heading angle - while still respect the constraints. Indeed, a more thorough inspection of the trajectories showed that, for the same Q, larger vehicles are more effective in changing the heading angle, and their flights also tend to last longer.

Bank angle profiles of optimal trajectories increase monotonically until they peak between 70 and 82 degrees, and at altitudes within the 64-74 km band. After this, the bank angle decreases with decreasing altitude. Optimal angle of attack profiles of long-range trajectories tend to drop quickly to zero or five degrees, where the L/D is maximum.

The Pareto front ensemble of the vehicles with maximum dimensions also provides some insight on the joint effect of β and r. Figure 17 shows that the combination of these two variables strongly drives the maximum cross-range a given waverider shape can achieve. For a fixed design Mach number, β is proportional to θ, whose tangent is, in turn, inversely proportional to L/D, as noted in [28]. With the simple aerodynamic model adopted here, r is proportional to D and does not influence L, so it is also inversely proportional to L/D. Hence, Fig. 17 grossly groups solutions by L/D: dark blue for high L/D, red for low L/D, and grey and light blue for medium L/D.

As expected, the fronts of the vehicles with higher L/D (minimum r and β) are broader, owing to the fact that solutions in the long cross-range end become accessible. Trajectories of high L/D configurations, however, tend to be dominated by the solutions of low L/D vehicles in the short and medium cross-range regions. A possible explanation

for this is that, for high L/D configurations, the optimiser has to explore and improve a wider range of solutions, thus dedicating less resources to the exploitation of trajectories.

Using the knee-point coordinates of each waverider shape, the second order models for the cross-range and heat load were fitted, leading to adjusted coefficients of determination of 0.946 for cross-range and 0.959 for heat load. The intercept and 95% confidence interval obtained for the cross-range objective and heat load objectives are 2176 ± 45 km and 0.682 ± 0.018 MJ, respectively.

The ratios P_f and the p-values were computed for each factor, and then used to group the terms into three categories:

- If $P_f \geq 0.5\%$ and the p-value is smaller than the significance level of 0.01, then term f is considered statistically significant and its effect on the response is relevant.
- If $P_f < 0.5\%$ and the p-value is smaller than the significance level of 0.01, then term f is considered statistically significant but its effect on the response is residual.
- If the p-value is larger than the significance level of 0.01, the term is considered statistically insignificant.

The P_f of terms in the statistically significant and relevant group are discriminated in Fig. 18. The bars are shown in red if the respective term has a negative sign (hence contributing to the minimisation of the objective), and blue otherwise. The vehicle length, the shock angle and the leading edge radius are driving both responses and the color distribution indicates conflicts. This is consistent with the analysis made for the ensemble of Pareto fronts.

The influence of the variables controlling the planform shape, e_1 and e_2, is very small for both objectives. The sensitivity to ω is also tenuous in both objectives, but stronger in Q, for which a small value is desirable (reflecting a compressed semi-circular shape). However, the relatively small sensitivity to ω does not imply that the effect of the leading edge cross section on the objectives is negligible, since β also affects its shape.

The sum of the P_f ratios of statistically significant terms is shown in the *Other SST* bar, while the equivalent figure for the statistically insignificant group is shown in the *Other SSI* bar. The plots also show the ratio S_E/S_T in the *Error* bar. The error can be used to assess the relevance of eventual non-modeled effects, such as three or higher-order factor interactions.

Angular rate constraints are inactive for the 189 trajectories used in the fitting process. The maximum $|\dot{\alpha}|$ recorded was 0.4 °/s, while the maximum $|\dot{\sigma}|$ was 1.7 °/s. The trim constraint is also inactive, and elevon-assisted trimming was needed only for a reduced number of shapes. This overall small trim effort may explain why the chord lengths of the control surfaces are absent from Fig. 18.

The γ constraint is active, but the most active constraints are the peak load factor and heat flux. Out of the 189 trajectories, only ten of them have a peak load factor away from the limit of 2.5. However, those same trajectories have a peak convective heat flux very close to the limit of 2 MW/m^2.

Since they are active constraints, the maximum values of heat flux, load factor and flight path angle found for the 189 runs were taken as observations to fit second order models, similarly to what was done with the cross-range and heat load

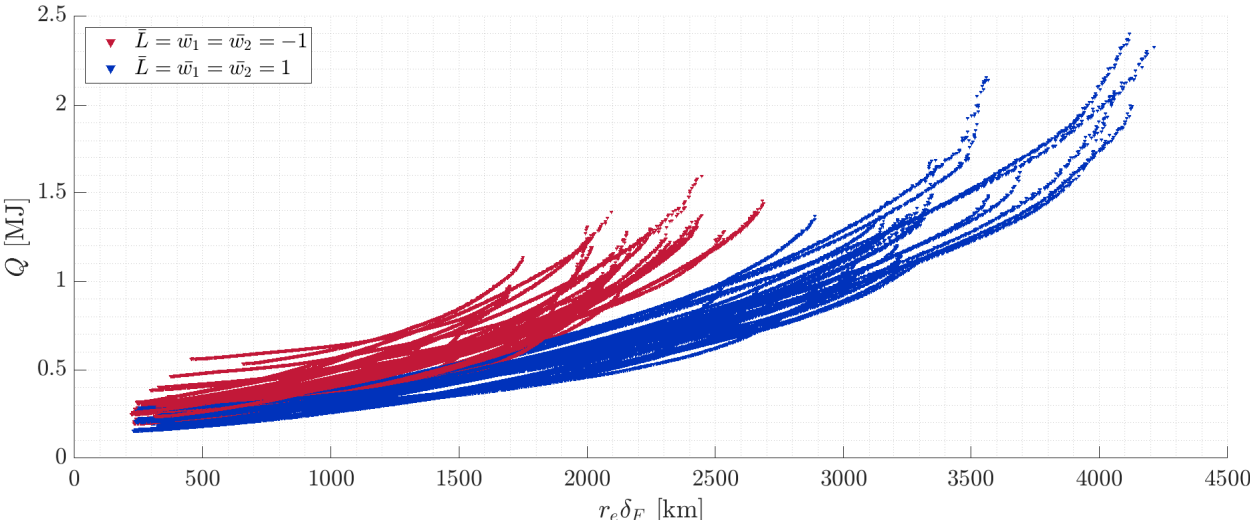

Fig. 16 Pareto-fronts of vehicles of minimum (red) and maximum (blue) planform dimensions. Each point corresponds to one optimal trajectory of its respective vehicle.

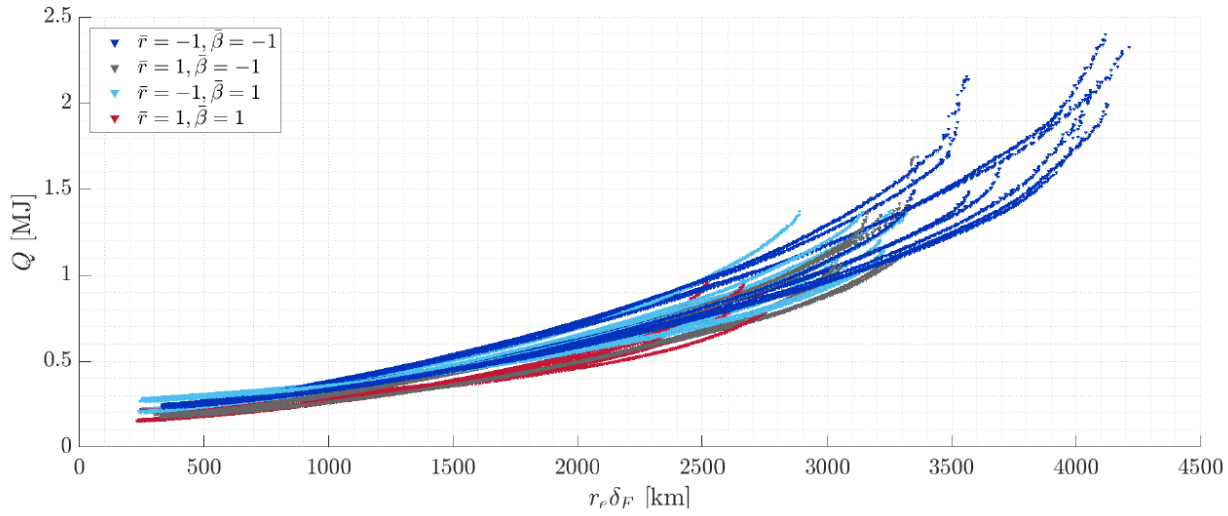

Fig. 17 Pareto fronts grouped by β, r combinations. Each point corresponds to one optimal trajectory of its respective vehicle.

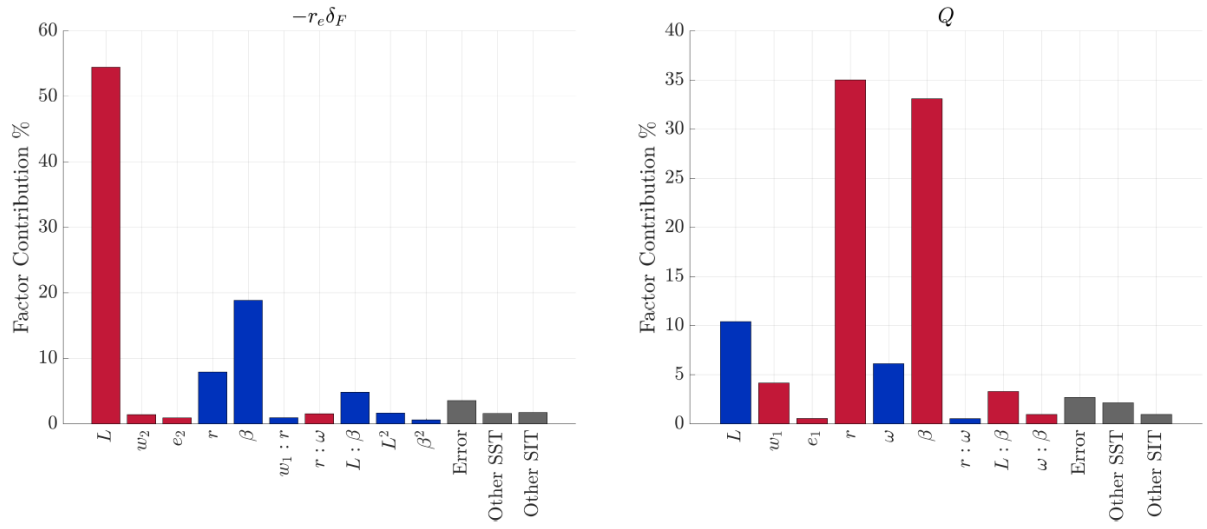

Fig. 18 Relative factor contributions to flight range and heat load.

Fig. 19 Predicted shapes for optimal cross-range (left) and heat load (right).

Table 2 Optimal coded design variables.

	$\bar{L}$	$\bar{w}_1$	$\bar{w}_2$	$\bar{e}_1$	$\bar{e}_2$	$\bar{r}$	$\bar{\omega}$	$\bar{\beta}$	$\bar{C}_e$	$\bar{C}_{bf}$
Optimal $r_e\delta_F$	1.00	1.00	1.00	-1.00	1.00	-1.00	-1.00	-1.00	-1.00	0.283
Optimal Q	-1.00	1.00	1.00	1.00	1.00	1.00	-1.00	1.00	1.00	-1.00

objectives. However, the adjusted coefficient of determination obtained are rather low (0.3537 for n and 0.1873 for γ) or, at best, reasonable (0.9071 for $\dot{q}_0$). It is not wise to optimise the shapes using inadequate models for the constraints, as feasible regions may be marked erroneously as unfeasible, potentially resulting in more optimal shapes to be discarded.

The unconstrained models were optimised individually using an interior point method, which produced the optimal configurations shown in Fig. 19. The coded design variables are shown in Table 3. Table shows that the observed heat load and cross-range for the two optimal shapes fall within the 95% confidence intervals of the predictions, which is indicative that the second order models are a good approximation of the true function landscapes. This claim is supported by Fig. 18, which shows the breakdown of the factor contributions to the two objectives. The error bar, which groups together the effects of non-modeled terms such as three-factor interactions, is smaller than 4%.

Table 3 Observed and estimated cross-ranges and heat loads for optimal shapes, with 95% confidence intervals.

	Estimated $r_e\delta_F$ [km]	Observed $r_e\delta_F$ [km]	Estimated Q [MJ]	Observed Q [MJ]
Optimal $r_e\delta_F$	2953 ±184	3004	0.941 ± 0.073	0.957
Optimal Q	1282 ± 184	1395	0.332 ± 0.073	0.389

V. Conclusions

For blunted hypersonic waveriders at small to moderate angles of attack, force coefficient predictions made with a novel modified-Newtonian/tangent-wedge hybrid method are more accurate than the standard modified-Newtonian model. Marginal improvements on the pitch moment coefficient were found.

The combined shape and trajectory optimisation approach proposed here builds up to response surfaces for cross-range and heat load with good quality. The respect for the multi-objective nature of the trajectory optimisation problem and the trajectory selection strategy adopted for the construction of the response surfaces make the latter a product that balances the two objectives. However, many Pareto-optimal trajectories are lost at the interface between shape and trajectory optimisation.

The optimal points estimated with the fitted surfaces are in good agreement with the observations, and the main factors driving the responses were clearly identified. Waveriders of larger dimensions are associated with higher S_{ref}/m and L/D ratios, and, consequently, tend to perform better than vehicles of smaller dimensions. Besides the vehicle dimensions, the shock angle and the leading edge radius are two key design drivers for the maximum cross-range a given waverider shape can achieve, with small values being desirable. This conflicts with what is desirable for heat-load.

The elevons are barely required for trimming, and usually small body flap deflections are sufficient. The sensitivity

of the responses to C_e and C_{bf} is thus very small, and the sizing of these surfaces could be left to a posterior study. The cross-range and heat load are also not very sensitive to terms containing the variables that control the wing/planform shape. As such, it is not reasonable to include them in the design space. Alternatively, a single control point or a wing with a constant sweep angle should be used and, once a commitment is made with the gross vehicle shape, the planform shape can be tweaked in a more detailed follow-up study.

Future research should investigate the stability and controllability characteristics of the waveriders, their relation to the shape features, as well as the impact that fin placement and design have on the cross-range, as these issues were overlooked here and may drive optimal designs into a different direction. It is also recommended to assess how sensitive the optimal trajectories are to viscous effects in the aerodynamics.

References

[1] Whitmore, S., and Dunbar, B., "Orbital Space Plane: Past, Present and Future," *AIAA/ICAS International Air and Space Symposium and Exposition: The Next 100 Years*, Vol. AIAA-2003-2718, 2003.

[2] Dirkx, D., and Mooij, E., *Conceptual Shape Optimization of Entry Vehicles Applied to Capsules and Winged Fuselage Vehicles*, Springer Aerospace Technology, 2017.

[3] Nonweiler, T., "Aerodynamic Problems of Manned Space Vehicles," *Journal of the Royal Aeronautical Society*, Vol. 63, 1959, pp. 521–528.

[4] Qu, Z., Xiao, H., Mingyun, L., Li, G., and Kai, C., "Numerical Study on Aerodynamic Performance of Waverider With a New Bluntness Method," *Proceedings of the Institution of Mechanical Engineers, Part G - Journal of Aerospace Engineering*, Vol. 235, No. 10, 2021, pp. 1225–1233.

[5] Borkowski, J., "Spherical Prediction-Variance Properties of Central Composite and Box-Behnken Designs," *Technometrics*, Vol. 37, No. 4, 1995, pp. 399–410.

[6] Kontogiannis, K., Cerminara, A., Taylor, N., Sóbester, A., and Sandham, N., "Parametric Geometry Models for Hypersonic Aircraft Components: Blunt Leading Edges," *20th AIAA International Space Planes and Hypersonic Systems and Technologies Conference*, Vol. AIAA-2015-3580, 2015.

[7] Lobbia, M., "Multidisciplinary Design Optimization of Waverider-derived Crew Reentry Vehicles," *Journal of Spacecraft and Rockets*, Vol. 54, No. 1, 2017, pp. 233–245.

[8] Hirschel, E., and Weiland, C., *Selected Aerothermodynamic Design Problems of Hypersonic Flight Vehicles*, AIAA and Springer, 2009.

[9] Dijkstra, M., Mooij, E., and Sudmeijer, K., "Trajectory Optimization to Support the Study of Hypersonic Aerothermodynamic Phenomena," *AIAA Atmospheric Flight Mechanics Conference*, Vol. AIAA-2013-4501, 2013.

[10] Anderson, J., *Hypersonic and High Temperature Gas Dynamics*, American Institute of Aeronautics and Astronautics, 2006.

[11] Lees, L., "Hypersonic Flow," *Journal of Spacecraft and Rockets*, Vol. 40, No. 5, 2003, pp. 700–735.

[12] Hankey, W., "Optimization of Lifting Re-entry Vehicles," Tech. rep., Aeronautical Systems Div Wright-Patterson Air Force Base, Ohio, 1963.

[13] Armellin, R., Lavagna, M., Starkey, P., and Lewis, M., "Aerogravity Assist Maneuvers: Coupled Trajectory and Vehicle Shape Optimization," *Journal of Spacecraft and Rockets*, Vol. 44, No. 5, 2007, pp. 1051–1059.

[14] Gregoire, J., and Krieger, R., "Aerodynamic Prediction Rationale for Advanced Arbitrarily Shaped Missile Concepts," *AIAA 18th Aerospace Sciences Meeting*, Vol. AIAA-80-0256, 1980.

[15] Gabeaud, A., "Base Pressures at Supersonic Velocities," *Journal of the Aeronautical Sciences*, Vol. 7, No. 8, 1950, pp. 525–526.

[16] Kays, W., and Crawford, M., *Convective Heat and Mass Transfer*, Tata McGraw-Hill Education, 1993.

[17] William, H., Simon, S., Craig, J., and Patrick, R., "Computational Fluid Dynamics Study of Optimized Hypersonic Leading Edge Geometries," *20th AIAA International Space Planes and Hypersonic Systems and Technologies Conference*, Vol. AIAA-2015-3509, 2015.

[18] Zhang, Q., and Li, H., "MOEA/D: A Multiobjective Evolutionary Algorithm Based on Decomposition," *IEEE Transactions On Evolutionary Computation*, Vol. 11, No. 6, 2007, pp. 712–731.

[19] Ishibuchi, H., Nojima, Y., and Doi, K., "On the Effect of Normalization in MOEA/D for Multi-objective and Many-objective Optimization," *Complex And Intelligent Systems*, Vol. 3, No. 4, 2017, pp. 279–294.

[20] Dijkstra, M., Mooij, E., and Sudmeijer, K., "Trajectory Optimization to Support the Study of Hypersonic Aerothermodynamic Phenomena," *AIAA Atmospheric Flight Mechanics Conference*, Vol. AIAA-2013-4501, 2013.

[21] Deb, K., Pratap, A., Agarwal, S., and Meyarivan, T., "A Fast and Elitist Multi-Objective Generic Algorithm: NSGA-II," *IEEE Transactions on Evolutionary Computation*, Vol. 6, No. 2, 2002, pp. 182–197.

[22] Wu, J., and Azarm, S., "Metrics for Quality Assessment of a Multiobjective Design Optimization Solution Set," *J. Mech. Des.*, Vol. 123, No. 1, 2001, pp. 18–25.

[23] Audet, C., Bigeon, J., Cartier, D., Digabel, S., and Salomon, L., "Performance Indicators in Multiobjective Optimization," *European Journal of Operational Research*, Vol. 292, No. 2, 2020, pp. 397–422.

[24] Brchnelova, M., and Mooij, E., "Validation and Application of the Axisymmetric Analogue Technique on Rapid Hypersonic Shape Optimisation," *AIAA Scitech 2022 Forum*, Vol. AIAA-2022-0146, 2022.

[25] McCartney, B., Prince, S., and Qin, N., "The Effect of Leading Edge Rounding on a Caret Waverider Configuration at Mach 8.2," 2016.

[26] Rodi, P., "Integration of Optimized Leading Edge Geometries Onto Waverider Configurations," *53rd AIAA Aerospace Sciences Meeting*, 2015, pp. AIAA–2015–1700.

[27] Cui, K., and Hu, S., "Shape Design to Minimize the Peak Heat-flux of Blunt Leading Edge," *51st AIAA Aerospace Sciences Meeting including the New Horizons Forum and Aerospace Exposition, Grapevine (Dallas/Ft. Worth Region), Texas, AIAA*, Vol. AIAA-2013-233, 2013.

[28] Starkey, R., and Lewis, M., "Simple Analytical Model for Parametric Studies of Hypersonic Waveriders," *Journal of Spacecraft and Rockets*, Vol. 36, No. 4, 1999, pp. 516–523.